Sukanya S. T.* and Jerine

A novel melanoma detection model: adapted K-means clustering-based segmentation process

https://doi.org/10.1515/bams-2020-0040
Received July 2, 2020; accepted October 21, 2020;
published online November 12, 2020

Abstract

Objectives: The main intention of this paper is to propose a new Improved K-means clustering algorithm, by optimally tuning the centroids.
Methods: This paper introduces a new melanoma detection model that includes three major phase's viz. segmentation, feature extraction and detection. For segmentation, this paper introduces a new Improved K-means clustering algorithm, where the initial centroids are optimally tuned by a new algorithm termed Lion Algorithm with New Mating Process (LANM), which is an improved version of standard LA. Moreover, the optimal selection is based on the consideration of multi-objective including intensity diverse centroid, spatial map, and frequency of occurrence, respectively. The subsequent phase is feature extraction, where the proposed Local Vector Pattern (LVP) and Grey-Level Co-Occurrence Matrix (GLCM)-based features are extracted. Further, these extracted features are fed as input to Deep Convolution Neural Network (DCNN) for melanoma detection.
Results: Finally, the performance of the proposed model is evaluated over other conventional models by determining both the positive as well as negative measures. From the analysis, it is observed that for the normal skin image, the accuracy of the presented work is 0.86379, which is 47.83% and 0.245% better than the traditional works like Conventional K-means and PA-MSA, respectively.
Conclusions: From the overall analysis it can be observed that the proposed model is more robust in melanoma prediction, when compared over the state-of-art models.

Keywords: GLCM; K-means clustering; melanoma detection; optimization; proposed LVP.

***Corresponding author: Sukanya**, Research Scholar, Noorul Islam Centre for Higher Education, Kanyakumari, India,
E-mail: stsukanya7@gmail.com
Jerine, Noorul Islam Centre for Higher Education, Kanyakumari, India,
E-mail: jerine@niuniv.com

Introduction

Melanoma is one of the most hurtful sorts of skin disease that starts in the colour cells (melanocytes) of the skin. Because of the overabundance disclosure of bright radiation from the sun, the skin cells are harmed and can influence the safe limit [1–4]. Snappy analysis and treatment can bring about a high chance of melanoma endurance [5]. At the same time, because of the similarity of skin injury types, the right conclusion is essential. The visual distinction between melanoma and generous skin injuries can be extremely slippery even for prepared clinical experts under unaided eye perception [6–9]. The different types of skin lesions are given in the following sections.

Normal vs. benign vs. malignant

The Normal mole is generally an evenly coloured black spot, tan or brown at the skin. It may be both flat and raised. The shape of the normal mole is round or oval. Moles are typically much less than 6 mm of ¼ inch, approximately the width of a pencil eraser.

Benign melanocytic lesions, is otherwise known as pigmented skin lesions or pigmented nevi. It generally has a round or oval shape with uniform colour and contour. Also, the course of evolution for those lesions, from junctional nevi to compound nevi to intradermal nevi, can be exposed with the aid of counting the number of nevi in numerous age corporations and analysing lesion specimens under a microscope. The range of nevi then increases unexpectedly to a mean count of 15–40 in childhood and early adulthood. The growth is associated with the amount of sun radiation the man or woman is exposed to in an unprotected state.

Melanoma skin cancer emerges when the colour-creating cells (melanocytes) display uncontrolled growth and become cancerous. Melanocytes are the skin cells, which produce the dark pigment known as melanin, the sunscreen. These cells hold to give melanoma, which obligates for the malignant growths acting in mixed shades of tan earthy and black colour. It is exceptionally uncommon in individuals with darkish pores and skin. The clinical examination depends upon on the surface of the lesion, colour and sort of outskirt. Benign is harmless, even as

(a) (b) (c)

Figure 1: Skin lesions. (a) Normal, (b) Benign and (c) Malignant.

malignant growth is perilous which needs quickly consideration. Figure 1 illustrates the skin lesions of normal, benign and malignant.

Dermoscopy [10, 11] also called as skin surface microscopy is a non-intrusive determination procedure that is utilized in the assessment and varieties of suspicious melanocytic injuries from melanoma. Clinical specialists use dermoscopy for determination [12–14]. In any case, the manual appraisal made by dermatologists from dermoscopy pictures is a protracted procedure and blunder inclined. Consequently, computerized calculations become a need to group melanoma, which aids in acquiring early conclusions about the disease and also helps in improving the diagnosing execution [2, 15]. Nonetheless, the indicative exhibition drops altogether when the specialists are not satisfactorily prepared [7, 8]. Suspicious skin lesions are also biopsied which is uncomfortable for the patient and turns out to be difficult to carry out diagnostic tests. Computer vision can play a significant role in the Diagnosis of Medical Image and many existing systems have proved it [16, 17]. So as to address the short stock of well-established technicians [18], particularly on creating accurate predictions, there have been a ton of looks into explicitly to create computerized picture examination frameworks to identify skin illness from dermoscopy pictures [19–21]. There are a few works in dermoscopy that have created indicative models for early recognition of melanoma [22].

The dermoscopic image segmentation assumes a significant job in improving the quality of the image utilized for prediction [23]. The Otsu colour thresholding [5] is a basic, yet amazing thresholding method utilized in a large portion of the research works. Further, in the case of classification, the computer-assisted diagnosis aids in determining melanoma. Typically, the most promising area of research in image classification is Machine learning, which makes an accurate prediction based on the quality of the image. The soft computing techniques get extensive awareness from researchers of diverse field [24–26]. The selection of appropriate model in the conventional optimization algorithms led to performance improvement [27–30]. A traditional ANN classifier utilizes back propagation calculation for preparing. The significant downside of this regular procedure is that the arrangement may get caught in the local minima rather than global minima. In order to eliminate this problem, the optimization algorithm can be introduced.

The major contributions of this research work are as follows.

- An Improved K-means clustering approach is proposed in this research work. Here, the optimal centroid selection is done by introducing a new optimization algorithm referred to as LAMN.
- This optimization algorithm makes the centroid selection more accurate by determining multi-objectives like **intensity diverse centroid, spatial map and frequency of occurrence.**
- To make the feature extraction mechanism more exclusive as well as significant, and novel LVP features referred as NVLVP is proposed.

The rest of the paper is organized as: Section 2 portrays about the literature works undergone in the recent past about the melanoma detection. Section 3 addresses the proposed melanoma detection framework: a compact description. Section 4 tells about the Improved K-means clustering: determining optimal centroids by the proposed LANM algorithm with multi-objective constraints. Further, the feature extraction: proposed NVLVP and GLCM are described in Section 5. The resultant acquired by the proposed work is discussed in Section 6. Finally, a strong conclusion is given to the current research work in Section 7.

Related works

In 2018, Do et al. [1] presented a new accessible mobile health-care solution to detect melanoma with the aid of the smartphone-captured visible-light images. The proposed localization algorithm encapsulated “skin/non-skin

detection, hierarchical segmentation and the combination of Otsu's method and MST method". Further, the colour variation as well as the irregularities in the borders of the skin image was quantified by utilizing the novel colour and border features.

In 2019, Warsi et al. [5] proffered multi-direction 3D CTF as a new approach for feature extraction from the collected dermoscopic images. The authors have detected the malignant melanoma from the collected dermoscopic image using the back propagation multilayer NN classifier. The evaluation of the presented work was done with the publicity available dataset PH^2 and the evaluation was accomplished in terms of "accuracy, sensitivity and specificity".

In 2019, Nida et al. [31] developed a deep learning-based automated melanoma region segmentation approach for determining melanoma from dermoscopic images. The authors have deployed the deep RCNN to detect a vast count of affected regions. In addition, the FCM clustering was implied to localize the formulated bounding boxes. Moreover, three major steps enclosed in this approach were: "skin refinement, localization of melanoma region and finally segmentation of melanoma".

In 2020, Thanh et al. [32] gained the help of an automatic image processing approach to construct a novel melanoma skin cancer detection framework. In the proposed framework, they have deployed adaptive principal curvature to pre-process the collected skin lesions dataset from ISIC. Then, the input images were segmented using the colour normalization, and the ABCD rule was introduced to extract the features from the segmented image.

In 2019, Tan et al. [33] established an intelligent decision support system for skin cancer detection. They represented the lesions of the skin image with the aid of the clinically important asymmetry, border irregularity, colour and dermoscopic structure features like Grey-Level Run Length Matrix, Local Binary Patterns, and Histogram of Oriented Gradients Operators. The extracted features were optimized using two enhanced PSO models. Moreover, they deployed the adaptive acceleration coefficients, multiple remote leaders, in-depth sub-dimension feature search, and re-initialization mechanisms to overcome the stagnation. Then, the hyper-parameter of the deep CNN was fine-tuned with PSO.

In 2019, Sabzevari et al. [34] have developed a synthetic ultra-high-resolution Millimetre-Wave Imaging system for early-stage detection of the Skin Cancer. The ultra-wide imaging bandwidth was split into 4 sub-bands and each sub-band was assigned to different imaging elements. That sub-band antenna transmitted and collected signals only from their respective sub-band, and further, these captured signals were merged and analysed to form the target image.

In 2018, Tan et al. [35] proposed an intelligent skin cancer diagnosis approach with the dermoscopic images using the PSO algorithm-based feature selection. The major intention behind the deployment of the proposed PSO lies in optimizing the features that are said to have discriminative characteristics in the case of both benign and malignant skin lesions. The search process was diversified using the probability distribution and dynamic matrix representations. Further, the evaluation of the proposed PSO variant with multiple skin lesions and diverse unimodal and multimodal benchmark functions extracted from UCI databases have shown superior performance over those of other advanced and classical search methods for identifying discriminative features.

In 2020, Zhang et al. [36] projected a novel approach for premature recognition of skin cancer using an optimal CNN. The authors have optimized the CNN with the help of the improved whale optimization algorithm.

In 2016, Jaworek-Korjakowska and Kleczek [37] presented a computer-aided approach for the classification of melanocytic lesions. They also focused on identifying the correct type of skin lesion like Spitz/Reed nevus, Clark nevus, melanoma, as well as a blue nevus. The performance was evaluated by utilizing classifiers viz., SVM decision tree, logistic regression and K-nearest neighbour algorithm. From the analysis, it is observed that the presented scheme achieved 92% accuracy with SVM.

In 2019, Goyal [38] introduced the fully automated deep learning ensemble technique. They trained the ensemble methods on the basis of DeeplabV3+ and Mask R-CNN. Finally, the result showed that the proposed ensemble method accomplishes high specificity and sensitivity in lesion boundary segmentation.

Presently, this disease remains an important health issue, and the need for effective clinical diagnosis has been a persistent challenge for dermatologists. Several techniques for image processing have already been established utilizing algorithms or mechanisms for identification, classification by means of different methods, and computational approaches used to solve medical problems. Table 1 shows the reviews on skin cancer detection methods. Among the interesting techniques disused in the literature, the features and challenges of each individual technique are portrayed here. AMD-SMIA in the study by Do et al. [1] is capable of segmenting as well as classifying the image with higher accuracy. The major challenge in this technique is higher cost consumption and lower

sensitivity and specificity. The overall accuracy, sensitivity as well as specificity are improved in CTF approach. But still, the system can be made more effective by improving the detection accuracy [5]. Further, RCNN + FCM in the study by Nida et al. [31] exhibit excellent segmentation performance. This technique needs to remove the artefacts as well as sharpen the image with no compensation in the quality of the image. In adaptive principal curvature + ABCD rule [32], the detection accuracy is higher. But, it detects the skin lesion with very low-intensity images only. Initially, the PSO method was deployed in the study by Do et al. [1], which presents minimal cost and highly flexible; however, it needs consideration on other datasets. Synthetic ultra-wideband imaging method was exploited in the study by Warsi et al. [5] that offers a maximum gain with higher bandwidth, but it requires consideration with the response of adjacent normal tissue subtracted from the response of tumour tissue. Moreover, PSO was deployed in the study by Nida et al. [31] that offers improved performance and it also presents minimal computational cost. Nevertheless, it needs consideration on optimal network parameters. Likewise, the CNN model was exploited in the study by Thanh et al. [32], which offers enhanced sensitivity and it is highly efficient. However, it has to concern with time utilization.

Proposed melanoma detection framework: a compact description

Proposed architecture

In this paper, a novel melanoma detection framework is introduced with three major phase's viz. **segmentation, feature extraction and detection**. Figure 2 illustrates the block diagram of the proposed melanoma detection model. The steps followed in this prediction approach are depicted below:

Step 1. Initially, the input skin image Im_{in} is subjected to an Improved K-means clustering algorithm, where the optimal centroid is already selected based on the training images. This selection is carried out by a new **LANM** algorithm based on multi-objective like **intensity diverse centroid, spatial map and frequency of occurrence.** The proposed algorithm is the conceptual improvement of standard LA. The optimally tuned centroids also fed as input along with the input image Im_{in}.

Step 2. Subsequently, from these segmented images ($\mathrm{Im}_{\mathrm{seg}}$), the features are extracted. More particularly,

Table 1: Features and challenges of traditional melanoma detection models.

Author [citation]	Methodology	Features	Challenges
Do et al. [1]	AMD-SMIA	– Captures the colour variation and border irregularity from the image. – Accurate segmentation and classification – more robust to over-fitting	– Need to improve the sensitivity and specificity
Warsi et al. [5]	CTF	– Improved accuracy, sensitivity, and specificity – overall computational complexity is low	– The system can be made computationally effective using improving the detection accuracy – Can employ classifiers for faster detection rates
Nida et al. [31]	RCNN + FCM	– good segmentation performance – good accuracy	– computationally extensive – Requires precise localization
Thanh et al. [32]	Adaptive principal curvature + ABCD rule	– high accuracy – good segmentation performance	– Detect the skin lesion with the very low intensity only
Tan et al. [33]	PSO	– Minimal cost – Highly flexible	– Requires more consideration on other datasets
Sabzevari et al. [34]	Synthetic ultra-wideband imaging method	– Maximum gain – High bandwidth	– Requires improvement in recall, accuracy, and precision.
Tan*et al.* [35]	PSO	– Reduced computational cost. – Improved performance.	– Needs consideration on optimal network parameters
Zhang et al. [36]	CNN	– Highly efficient – Enhanced sensitivity	– No consideration on the processing time – Prone to noise

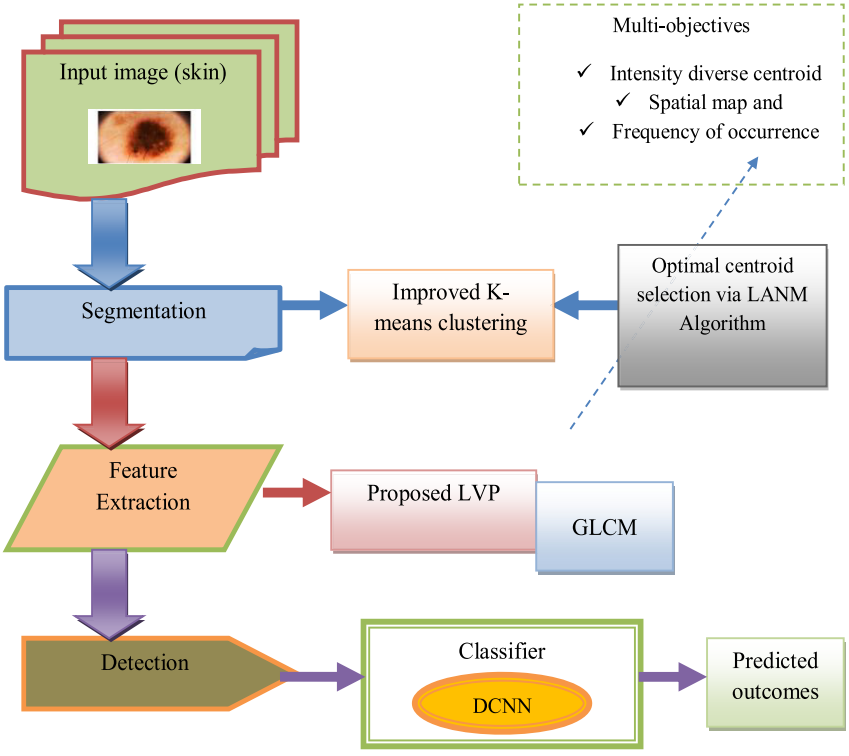

Figure 2: Block diagram of Proposed Melanoma Detection Framework.

proposed **LVP** (Fe^{LVP}) **and GLCM** (Fe^{GLCM}) are extracted. The final features $Fe=Fe^{LVP} + Fe^{GLCM}$ are subjected for the melanoma detection process.

Step 3. For this, **Deep Convolutional Neural Network (DCNN)** is used. The results from DCNN will determine the accurate results on the presence or absence of the melanoma.

Improved K-means clustering: determining optimal centroids by proposed LANM algorithm with multi-objective constraints

Improved K-means clustering

The K-means algorithm is also defined as the partition-based cluster analysis approach. As per the algorithm, initially selects cluster centres k (centroid), then evaluate the distance among each object and each k and assign it to the nearest cluster, repeat the mentioned process till the final criterion gets converged [39]. However, in the proposed work, rather than selecting the centroids randomly, it is planned to select the optimal centroid by a new optimization algorithm. In fact, the selection process of centroids might be carried out under the training process via training images. While testing, the input image Im_{in} and the respective optimal centroids are given as the input for differentiating the ROI and Non-ROI region since in this work $k_j;j=1,2$. Further, the optimal selection of centroids is carried out based on certain objectives that are described in the subsequent section. The steps followed in the proposed Improved K-means algorithm is as follows:

Step 1. Getting Input Image Im_{in} and the optimal centroids selected initially k.

Step 2. Evaluate the distance between each object and centroids k.

$$d(p,k) = \sum_{i=1}^{n} (p_i - k_j)^2 \quad (1)$$

Step 3. Clustering based on the minimum distance.

Step 4. Repeat the steps, until the criteria get converged.

Optimal initial centroids by LANM

In the current research work, three objectives are proposed to evaluate the quality of initial centroids, while the

majority of the initial centroid selections are based on distance (considers only intensity) [39]. All these three objectives together act as a base for the optimal centroids selection in the LAMN algorithm. The solution given to the algorithm is illustrated in Figure 3, where k_1 and k_2 are two centroids generated within the bounds 0 and 255.

As mentioned, the selection takes place on the basis of three major objectives given below:

- Intensity-diverse centroid
- Spatial map
- Frequency of occurrence

In prior to fitness computation, it is essential to sort the input image Im_{in} in ascending order on the basis of its pixel intensity (P_m). The pixels $\mathrm{P}_{(N\times M)e}$ in the X,Y coordinate corresponding to N rows and M columns are sorted, and the unique (Q) as well as frequency of occurrence (F) of the pixels are evaluated as per Eqs. (2) and (3). The symbol e denotes the overall pixels in the image and it varies from e=1,2, … , L. Here, L denotes the count of unique pixel intensities q denotes the intensity of the pixels and f is the frequency of each intensity.

$$Q = \{q_1, q_2, \ldots, q_L\} \tag{2}$$

$$F = \{f_1, f_2, \ldots, f_L\} \tag{3}$$

Objective 1. Intensity-diverse centroid

The mathematical formula for Intensity-diverse centroids expressed in Eq. (4). Here, k_1 and k_2 are the two solutions and the integer 255 represents the maximal bound of the solution space.

$$Obj_1 = 1 - \frac{|k_1 - k_2|}{255} \tag{4}$$

Further, while compared to Obj_2 and Obj_3, the first objective Obj_1 is more significant, as it highly influences the final objective. For illustration: Obj_1=1 (poor) and Obj_2=Obj_3=0 (good), the final objective is high. On the other hand, Obj_1=0 (good) and Obj_2=Obj_3=1 (poor), the final objective is low and hence the prediction accuracy gets enhanced.

Objective 2. Spatial map (*S*)

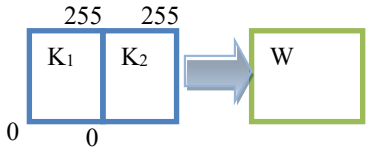

Figure 3: Solution encoding.

The location of (Q) that are closer to the centroids (k_1,k_2) are computed with respect to the threshold value T. The resultant is denoted as $Q^*_{i=1,2}$. This is mathematically defined in Eq. (5) and Eq. (6), respectively.

$$Q_1^* = Q \| k_1 - Q \| < T \tag{5}$$

$$Q_2^* = Q \| k_2 - Q \| < T \tag{6}$$

Further, the standard deviation (SD) is computed for Q_1^* in both the X,Y coordinate as per Eq. (7) and Eq. (8), respectively, for k_1. Similarly, compute D_{2X} and D_{2Y} for k_2 as per Eq. (9) and Eq. (10).

$$D_{1X} = SD(X(Q_1^*)) \tag{7}$$

$$D_{1Y} = SD(Y(Q_1^*)) \tag{8}$$

$$D_{2X} = SD(X(Q_2^*)) \tag{9}$$

$$D_{2Y} = SD(Y(Q_2^*)) \tag{10}$$

Then, the spatial distribution D_1 is computed for k_1 by taking the average of D_{1X} and D_{1Y}, as per Eq. (11). Similarly, spatial distribution D_2 is also computed for k_2 as per Eq. (12).

$$D_1 = \frac{D_{1X} + D_{1Y}}{2} \tag{11}$$

$$D_2 = \frac{D_{2X} + D_{2Y}}{2} \tag{12}$$

The spatial map (S) is evaluated by taking the average of the spatial distribution D_1 and spatial distribution D_2. In addition, $N \times M$ represents the area of the image in Eq. (13).

$$Obj_2 = S = \frac{D_1 + D_2}{2(N \times M)} \tag{13}$$

Objective 3. Frequency of occurrence

R_1 and R_2 denotes the frequency of the occurrence of Q_1^* and Q_2^*, respectively, which is mathematically defined in Eqs. (14) and (15).

$$R_1 = Average(F(Q_1^*)) \tag{14}$$

$$R_2 = Average(F(Q_2^*)) \tag{15}$$

Moreover, the overall occurrence of the frequency of pixel, which is the 3rd objective of the current research work is computed using Eq. (16).

$$Obj_3 = 1 - \min\left(\frac{R_1}{255}, \frac{R_2}{255}\right) \tag{16}$$

The overall objective (Obj) of the current research work is mathematically defined in Eq. (17). Here, the denominator indicates the scaling factor S_{factor} and in this work, it is fixed as 2.

$$Obj = \min\left[Obj_1 + \left(\frac{Obj_2 + Obj_3}{S_{\text{factor}}} \right) \right] \tag{17}$$

Proposed LANM algorithm

Lion Algorithm [40–44] is based on the social behaviour of the lion such as the territorial defence and territorial takeover. The nomads take over the pride in the territorial defence. In order to enhance the existing model with respect to convergence rate, this work extends the model including a new mating process, thereby named as LANM. The four phases of the proposed algorithm are given as follows: (a) Pride Generation, where initialization of the pride takes place, (b) Proposed Mating process, where new solutions are derived, (c) Territorial Defence and (d) Territorial Takeover.

Pride Generation: This is the initialization step, where the initialization of lion, lioness and nomads are depicted as W^{male}, W^{female} and W_1^{nomad} carried out. The pride is generated by the male lion W^{male} and its lioness W^{female}.

Fitness Evaluation: Here, the fitness of the male lion W^{male}, its lioness W^{female}, and nomad W_1^{nomad} are determined and the fitness evaluated W^{male}, W^{female} and W_1^{nomad} are denoted as $fn(W^{\text{male}})$, $fn(W^{\text{female}})$ and $fn(W_1^{\text{nomad}})$, respectively. Also, an assumption is made, fn^{ref}=$fn(W^{\text{male}})$ and N_g=0. The term N_g describes the generation counter, which helps in evaluating the termination process.

Fertility Evaluation: The productiveness of the territorial lion and lioness are securitized and the fertility of them is generated as the outcomes [40]. At the end of the fertility evaluation process, the updated female lion is generated and it is denoted as $W^{\text{female+}}$, given in Eq. (18). The random integer is depicted as h and $w_l^{\text{female+}}$ and $w_h^{\text{female+}}$ are lth and hth elements of $W^{\text{female+}}$. The mathematical formula for $w_h^{\text{female+}}$ is shown in Eq. (19) and the term ∇ in Eq. (20) depicts the female update and r_1, r_2 are denoted as random integers.

$$W^{\text{female+}} = \begin{cases} w_h^{\text{female+}} ; \text{if } l = h \\ w_1^{\text{female}} ; \text{otherwise} \end{cases} \tag{18}$$

$$W_h^{\text{female+}} = \min\left\lfloor w_h^{\max}, \max\left(w_h^{\min}, \nabla_h\right)\right\rfloor \tag{19}$$

$$\nabla_h = \left\lfloor w_{fh}^{\text{female}} + (0.1r_2 - 0.05)\left(w_h^{\text{male}} - r_1 w_h^{\text{female}}\right)\right\rfloor \tag{20}$$

Proposed Mating: Crossover and mutation are the two primary steps in the mating process. In the traditional LA algorithm, four cubs are generated from the mutation process and four cubs from the cross over mechanism. All these together fill the cub pool. But, in the proposed LAMN model to make the optimal centroid selection more precise and elite, 8 new cubs are generated using the cross over $W^{\text{cubs(cross)}}$ process and 8 new are produced with the aid of the mutation process $W^{\text{cubs(mut)}}$. Then, the average of this considered being the final cubs as defined in Eq. (21).

$$W^{cubs} = \frac{W^{cubs(mut)} + W^{cubs(cross)}}{2} \tag{21}$$

Further, W^{cubs} are subjected to uniform mutation at the rate Mut_r. Subsequently, the extraction of the male cub $W^{\text{male\_cub}}$ and female cub $W^{\text{female\_cub}}$ takes place based on the first and second-best fitness of W^{new}, respectively, in the gender clustering process. After the selection of the male cub $W^{\text{male\_cub}}$ and female cub $W^{\text{female\_cub}}$, their ages A_{cub} is set to zero. The maximum age of the cub is denoted as $A_{\max}$.

Cub Growth Function: In this process, $W^{\text{male\_cub}}$ and $W^{\text{female\_cub}}$ are absorbed to uniform random mutation with the rate of M_r. In case, if the mutated cub is strong, then the old cub is restored with a new cub and the ages A_{cub} are increased to one at each of the update processes.

Territorial defence: The nomad coalition is created by means of following the survival fight, pride and nomad coalition updates in the territorial defence. This formulation of the nomad coalition is based on the capability of the succeeding W^{nomad}. On the basis of the following criteria, the selection of the winning nomad is accomplished.

$$fn\left(W^{\text{e\_nomad}}\right) < fn\left(W^{\text{male}}\right) \tag{22}$$

$$fn\left(W^{\text{e\_nomad}}\right) < fn\left(W^{\text{male\_cub}}\right) \tag{23}$$

$$fn\left(W^{\text{e\_nomad}}\right) < fn\left(W^{\text{female\_cub}}\right) \tag{24}$$

Territorial takeover: The process of terrestrial take over is accomplished, when $A_{\text{cub}} \geq A_{\max}$. In case, if this condition is not met, the process from cub growth function gets repeated. This process provides territory $W^{\text{male\_cub}}$ as well as $W^{\text{female\_cub}}$, once they grow up and become matured and stronger than W^{male} and W^{female}.

Termination criteria: The final stage of LA is the termination criterion and storage of W^{male} and $f(W^{\text{male\_cub}})$ takes place. The process of fertility evaluation undergoes a recap when the condition N_g>$N_g^{\max}$ is not satisfied. The term N_g and $N_g^{\max}$ depicts the number of function evaluations and the maximum count of function computations. The pseudo-code of the proposed LANM algorithm is depicted in Algorithm 1.

Algorithm 1: Pseudo- code of LANM model

Step 1: Pride generation	W^{male}, W^{female} and W^{Nomad}, respectively are initialized.
Step 2	$fn(W^{male})$, $fn(W^{female})$ and $fn(W^{nomad})$, are computed
Step 3	Set objective 1(Intensity- diverse centroid) as per Eq. (4)
Step 4	Set objective 2 (spatial map) as per Eq. (13)
Step 5	Set objective 3 (frequency of occurrence) as per Eq. (16)
Step 6	$f(W^{male})=fn^{ref}$ is assigned and $N_g=0$
Step 8	Accumulate the value of W^{male} and $fn(W^{male})$and perform fertility evaluation
Step 9: Proposed Mating process	**(i)Perform cross over and mutation, and generate the cub pool** **(ii) In the cub pool, 8 cubs are generated by mutation and 8 by cross over** **(iii) The average is computed for these 16 cubs as per Eq. (21)**
Step 10: Gender clustering	To attain $W^{male_cub}$and W^{female_cub}
Step 11	Assign age of cub as $A_{cub}=0$
Step 12	cub growth function is executed
Step 13	Territorial defence is performed, while the resultant of defence result 0, go to step 8
Step 14	If $A_{cub}<A_{max}$, then go to step 9.
Step 15: Territorial takeover	Update W^{male} and W^{female}
Step 16	Increase N_g by one
Step 17	If the termination criteria is not satisfied, go to step 9, otherwise terminate the process.

Feature extraction: proposed LVP and GLCM

The segmented image Im_{seg} is subjected under feature extraction, where the features such as GLCM and proposed LVP are extracted.

Existing LVP

The micropattern's distinctive 2D spatial structures can be depicted in terms of the referenced pixel and its neighbourhoods with various pair-wise directions using the LVP descriptor [45]. The vector directional value for the segmented image Im_{seg} is denoted as $V_{E,\beta}(H_C)$. The referenced pixel is symbolized as H_C and along with the directional variation, the index angle is denoted asβ. Further, the distance between the adjacent pixels and the reference pixel along is denoted as E. At H_C, the direction value of a vector is defined mathematically as per Eq. (25).

$$V_{E,\beta}(H_C) = \left(\mathrm{Im}_{seg}(H_{E,\beta}) - \mathrm{Im}_{seg}(H_c)\right) \tag{25}$$

When, E=1, the vector is said to be the first-order derivative of LDP and LTrP. Then, along the 1D direction, the implicit characteristics are acquired in the 1D direction. The encoding of LVP at H_C along the direction of β is depicted as per Eq. (26).

$$\mathrm{LVP}_{G,\widehat{R},\beta}(H_C) = \left\{ \begin{array}{l} s_5\left(U_{E,\beta}\left(H_{1,\widehat{R}}\right), U_{E,\beta+45^0}\left(H_{1,\widehat{R}}\right), U_{E,\beta}(H_c), U_{\beta+45^c,K}(H_C)\right), \\ s_5\left(U_{E,\beta}\left(H_{2,\widehat{R}}\right), U_{E,\beta+45^0}\left(H_{2,\widehat{R}}\right), U_{E,\beta}(H_c), U_{E,\beta+45^0}(H_c)\right), \ldots \\ s_5\left(U_{E,\beta}\left(H_{g,\widehat{R}}\right), U_{E,\beta+45^0}\left(H_{g,\widehat{R}}\right), U_{E,\beta}(H_c), U_{E,\beta+45^0}(H_c)\right) \end{array} \right\} \times |g = 1, 2, \ldots, G; \widehat{R} = 1 \tag{26}$$

The transform ratio is adopted by s_5 (',') and it is computed with the help of the referenced pixel's vector pairwise direction. This is undergone to transform the neighbourhood β- direction value to the direction of $\beta + 45^\circ$. The mathematical formula for s_5 (',') is depicted in Eq. (27).

$$s_5\left(\left(U_{E,\beta}(H_{g,R}), U_{E,\beta+45^0}(H_{g,R}), U_{E,\beta}(H_C), U_{E,\beta+45^0}(H_C)\right)\right) = \begin{cases} 1 & if\ U_{E,\beta+45^0}(H_{g,R}) - \left(\dfrac{U_{E,\beta+45^0}(H_C)}{U_{E,\beta}(H_C)} \times U_{E,\beta}(H_{g,R})\right) \geq 0 \\ 0 & \text{else} \end{cases} \tag{27}$$

At H_C, the LVP is said to be the concentration of four 8-bit binary patterns and it is depicted as $\mathrm{LVP}_{G,R}(H_C)$ as per Eq. (28).

$$\mathrm{LVP}_{G,R}(H_c) = \mathrm{LVP}_{G,R,\beta}(H_c) | \beta = 0^\circ, 45^\circ, 90^\circ \text{ and } 135^\circ \tag{28}$$

Drawbacks

- Labelling of the binary pattern of mean patterns takes threshold as "0" in Eq. (27).
- The thresholding mechanism is static and the quality of the image is invariant.
- It is insensitive to image quality.

Thus, there is a necessity to develop a new LVP based feature extraction approach.

Proposed LVP

The efficiency of the LVP-based feature extraction technique depends on proper threshold selection for the segmented image Im_{seg}. In this paper, a thresholding based new NVLVP approach is introduced. Here, the threshold

(Th) is computed with the help of the qualitative variance (Var) of the neighbourhood. It uses the variation around the median. The mathematical formula for threshold (Th), based on the mode of neighbours (fr_m) and mode of the zth pixel (fr_z)is depicted in Eq. (29).

$$Th = \sum_{b=1}^{N_P} (fr_m - fr)_z \tag{29}$$

The basic standardization properties of qualitative variance [46] that need to be satisfied during the analysis of the nominal data are:

- Variation (Var) fluctuates between 0 and 1.
- When, all the cases are said to come under a single category, Var=0.
- When, all the cases are said to be distributed evenly across all the categories, Var=1.

Particularly, all the standardized indices' values aren't dependent on the count of the samples or the categories. Further, the index that is closely related to the uniform distribution has a larger variance. Along with the categories, when the frequency difference is larger, the variance is said to be smaller.

Feature: According to Eq. (29), the threshold Th dynamically varies for every pixel based on the texture contents of the image, whereas the existing LVP has a constant threshold of "0" for all the pixels.

Lemma 1. The neighbourhood variant acts as LVP, when the neighbourhood exhibits extreme similarity and dissimilarity. Hence, the proposed model is referred as NVLVP.

Proof: A sub-image of Im_{seg} is taken into consideration. It is in the form of a 3×3 matrix (in Figure 4) with count of neighbouring pixels No_p=8.

Case 1. Extreme Similarity: Here, x_1=x_2=x_3=x_4=x_5=x_6=x_7=x_8 (i.e.) x_i=x_j j=1, 2, …, 8 and i=1,2, … ,8. In this case, the value of fr_m=fr_z:i=1, 2, …, 8. Hence, Th=0 (=LVP). In case of extreme similarity between the neighbourhood pixels, the threshold value becomes 0 and LVP has a constant threshold of "0" for all the pixels.

x_4	x_3	x_2
x_5	x_0	x_1
x_6	x_4	x_8

Figure 4: 3 × 3 matrix of a sub-image from the segmented image.

Case 2. Extreme dissimilarity: Here, x_1≠x_2≠x_3≠x_4≠x_5≠x_6≠x_7≠x_8 (i.e.) $x_i \neq x_j$ j=1, 2, …, 8 , i=1,2, … ,8 and i≠j. In this case, the value of f_m=f_i=1. Hence, the threshold Th=0 (=LVP). When the neighbourhood pixels aren't similar to each other, the threshold Th is set as 0 and its LVP is set as 0. (i.e. When Th=0, its LVP). Apart from these both cases, the threshold value gets varied on the basis of the pixels groups.

Thus, a strong conclusion can be acquired from this lemma that, the neighbourhood variant acts as LVP, if and only if the neighbourhood variant exhibits either extreme similarity or extreme dissimilarity. Both cases (case 1 and case 2) corresponding to extreme similarity and extreme dissimilarity exhibits that the threshold value isn't fixed and it depends on the texture content of the image.

An illustration for threshold computation is depicted below: in Figure 4, the 3 × 3 matrix having neighbouring pixels No_p=8. Let, x_1=x_2=x_3; x_4=x_5:x_6=x_7=x_8. The frequency of each individual pixel is given in Figure 5.

From Figure 5, the mode=3(maximum frequency) Th=(mode – x_1) + (mode – x_2) + (mode – x_3) + (mode – x_4) + (mode – x_5) + (mode – x_6) + (mode – x_7) + (mode – x_8). The impact of average threshold over the pixel groups is exhibited graphically in Figure 6.

As discussed above, when the count of neighbouring pixels arranges around the centre pixel is similar (case 1), they form a single pixel group and their average threshold

Neighbour	x_1	x_2	x_3	x_4	x_5	x_6	x_7	x_8
Frequency	3	3	3	2	2	3	3	3

Figure 5: Frequency of pixel occurrence: An illustration.

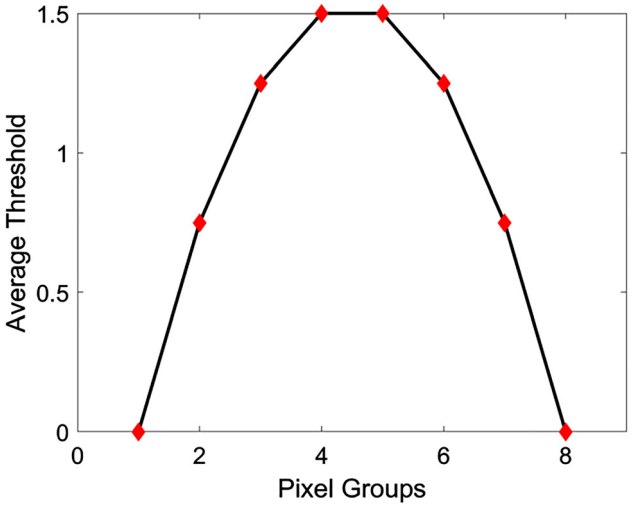

Figure 6: Pixel group vs. threshold.

is 0. Further, when the similarity between the pixels varies, the count of pixel group formation count increases, and this in turn increases the average threshold. On the other hand, in case of extreme dissimilarity, the threshold again falls to its lowest value (0). This is clearly exhibited in Figure 6.

Moreover, the necessity of the proposed thresholding-based NVLVP can be understood from the statistical evaluation determined in terms of pixel groups over a threshold value. Typically, this evaluation is done by feeding 5 sample images as input to the proposed NVLVP algorithm. The statistical evaluation (mean, minimum, maximum, median, and standard values) in the threshold value corresponding to the pixel group formation is tabulated in Table 2. The extracted NVLVP features are denoted as Fe^{LVP}.

GLCM

Further, the GLCM features are also extracted. GLCM (Grey-Level Co-event Matrix) is the factual technique that is deployed in this research work for evaluating the spatial relationship between the pixel [47]. The brief explanation of GLCM features is denoted in Table 3. The features extracted from GLCM are denoted as Fe^{GLCM}.

The obtained features together are summed up as $Fe{=}Fe^{\mathrm{LVP}} + Fe^{\mathrm{GLCM}}$.

Table 2: Impact of pixel groups on the threshold value.

Constraints	Mean	Min	Max	Median	Standard deviation
Pixel groups	1.2167	0	3	1	0.47518
Threshold	0.16447	0	1.5	0.15	0.35949

DCNN-based classification

Here, the extracted features *Fe* from the previous phase are subjected to the Deep CNN model [48]. In general, DCNN is a well-known deep learning model that is being exclusively deployed in recent studies for better classification accuracy. The DCNN encapsulates diverse layers: "convolutional layer, pooling layer and fully connected layers". A massive count of convolution kernels is available in the convolution layer and these convolution kernels aids in evaluating the diverse feature maps. In particular, in the feature map, each of the neurons is connected its neighbours in the previous layer and this form of linkage is denoted as neuron's receptive field. Further, with the aid of diverse kernels, the complete feature maps can be acquired. At the location (u, v) in the sth layer of the corresponding oth feature map, the feature values are computed using Eq. (30).

$$Z^{s}_{u,v,o} = Wt^{s^T}_{o} J^{s}_{u,v} + B^{s}_{o} \tag{30}$$

Table 3: GLCM features.

S.No.	Features	Mathematical expression
1	Energy	$E = \sum_a \sum_b s^2_{ab}$, here s_{ab} is the (a, b)th entry in GLCM
2	Entropy	$Entropy = -\sum_a \sum_b s_{ab} \log_2 s_{ab}$
3	Contrast	$Con = \sum_a \sum_b (a-b)^2 s_{ab}$
4	Variance	$V = \sum_a \sum_b (a-\mu)^2 s_{ab}$, where μ specifies the mean of s_{ab}
5	Homogeneity	$H = \sum_a \sum_a \frac{1}{1+(a-b)^2} s_{ab}$
6	Correlation	$C = \frac{\sum_a \sum_b (ab) s_{ab} - \mu_x \mu_y}{\sigma_x \sigma_y}$, where σ_x,σ_y, μ_x,μ_y are the std deviations and mean of s_x,s_y
7	Sum average	$SA = \sum_{a=2}^{2N_s} a.s_{x+y}(a)$, where N_s indicates the varied grey levels in image.
8	Sum entropy	$SE = \sum_{a=2}^{2N_s} s_{x+y}(a) \log\{s_{x+y}(a)\}$
9	Sum variance	$SV = \sum_{a=2}^{2N_s} (a - SE)^2 s_{x+y}(a)$
10	Difference variance	DV=variance of s_{ax-y}
11	Difference entropy	$DE = \sum_{a=0}^{N_{s-1}} s_{x-y}(a) \log\{s_{x-y}(a)\}$
12	MCC (2nd higher eigen value of Q)$^{0.5}$	$\mathrm{MCC} = \sum_k \frac{g(a,k) g(b,k)}{g_x(a) g_y(k)}$
13	Information measures of correlation 1	$\mathrm{IMC1} = \frac{HXY - HXY1}{\max\{HX, HY\}}$
14	Information measures of correlation 2	$IMC2 = \sqrt{(1 - \exp[-2.0[HXY2 - HXY]])}$, where $HXY = -\sum_a \sum_b s_{ab} \log_2 s_{ab}$ $HXY1 = -\sum_a \sum_b s_{\mathrm{ab}} \log_2 \{s_x(a) s_y(b)\}$

Here, the notation Wt_o^s denotes the weight vector, and the bias term corresponding to oth filter in the sth layer are represented as B_o^s. In addition, at the cantered location (u, v) of sth layer, the patched input is denoted as $J_{u,v}^s$. In CNN, the non-linearity is introduced by the activation function act(•). The activation value $(\text{act}_{u,v,o}^s)$ corresponding to the convolutional features $Z_{u,v,o}^s$ is computed using Eq. (31).

$$act_{u,v,o}^s = act\left(Z_{u,v,o}^s\right) \tag{31}$$

Pooling layer: "Pooling layers in the DCNN perform the downsampling operations with the outcomes acquired from the convolutional layers". In the pooling layer, each of the feature maps is connected to its preceding feature maps in the convolutional layer. Then, for every pooling function pool(•) corresponding to $\text{act}_{,,o}^s$, the value of $U_{u,v,o}^s$ is computed using Eq. (32).

$$U_{u,v,o}^s = pool\left(\text{act}_{u,v,o}^s\right), \forall (u,v) \in \Re_{u,v} \tag{32}$$

The classification job is accomplished in the final layer of DCNN, the output layer. The loss of CNN is depicted as Loss and it is determined using Eq. (33).

$$Loss = \frac{1}{N}\sum_{n=1}^{N} s\left(\theta;\, U^{(n)}, A^{(n)}\right) \tag{33}$$

The overall parameter corresponding to Wt_o^s and B_o^s is denoted as θ. Here exists N count of input–output relations. The nth input data, the corresponding target labels, and the output of CNN is represented as, $U^{(n)}$ and $A^{(n)}$, respectively. Figure 7 depicts the block diagram of CNN.

Results and discussions

Experimental setup

The proposed melanoma detection model was implemented in **MATLAB** and the resultant acquired is recorded. The simulation work was taking place using PH^2 database and ISIC database. The dataset of skin images utilized for evaluation is downloaded from "https://www.fc.up.pt/addi/ph2%20database.html" [Access date: 2020-05-12] and "https://www.isic-archive.com/#!/topWithHeader/tightContentTop/about/isicArchive" [Access date: 2020-05-19]. Figure 8 and Figure 9 show the image results of both normal as well as abnormal sample images, respectively. The performance of the proposed work was compared over other traditional models with respect to positive and negative measures like "accuracy, sensitivity, specificity, precision, FPR, FNR and FDR, respectively".

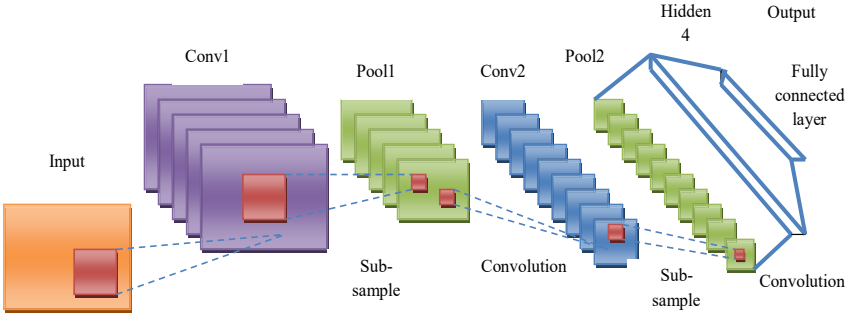

Figure 7: Architecture of DCNN.

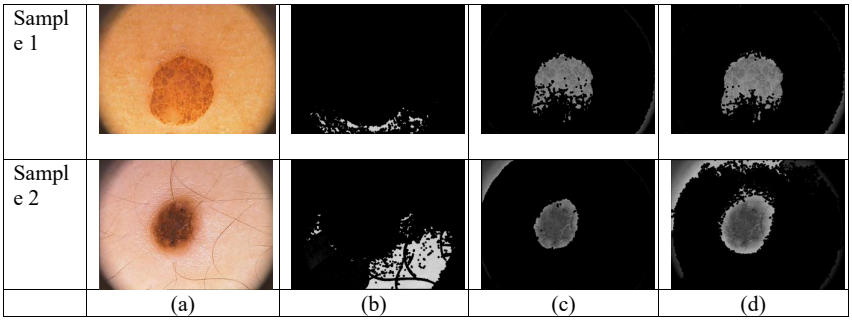

Figure 8: Segmentation results. (a) Normal input image (samples), (b) Conventional K-means, (c) PA-MSA (d) Proposed K-means with LANM-based segmentation.

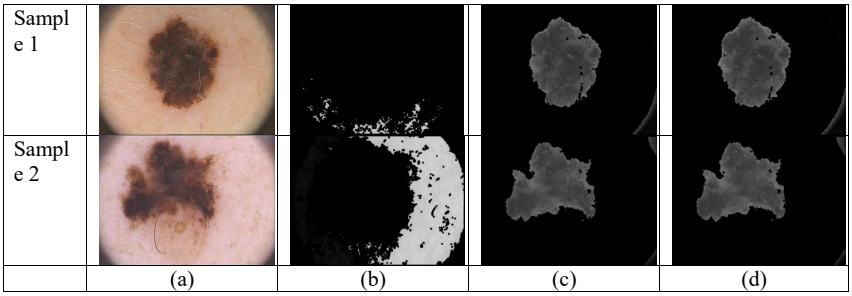

Figure 9: Segmentation results. (a) Abnormal input image (samples), (b) Conventional K-means, (c) PA-MSA and (d) proposed K-means with LANM-based segmentation.

Dataset description

PH^2 database

"The dermoscopic images were obtained at the Dermatology Service of Hospital Pedro Hispano (Matosinhos, Portugal) under the same conditions through the Tuebinger Mole Analyser system using a magnification of 20×. They are 8-bit RGB colour images with a resolution of 768 × 560 pixels. This image database contains a total of 200 dermoscopic images of melanocytic lesions, including 80 common nevi, 80 atypical nevi and 40 melanomas. The PH^2 database includes medical annotation of all the images namely medical segmentation of the lesion, clinical and histological diagnosis, and the assessment of several dermoscopic criteria (colours; pigment network; dots/globules; streaks; regression areas; blue-whitish veil)".

ISIC database

"Melanoma Project is an academia and industry partnership designed to facilitate the application of digital skin imaging to help reduce melanoma mortality. When recognized and treated in its earliest stages, melanoma is readily curable. Digital images of skin lesions can be used to educate professionals and the public in melanoma recognition as well as directly aid in the diagnosis of melanoma through teledermatology, clinical decision support and automated diagnosis. Currently, a lack of standards for dermatologic imaging undermines the quality and usefulness of skin lesion imaging. ISIC is developing proposed standards to address the technologies, techniques and terminology used in skin imaging with special attention to the issues of privacy and interoperability (i.e. the ability to share images across technology and clinical platforms). Also, ISIC has developed and is expanding an open-source public access archive of skin images to test and validate the proposed standards. This archive serves as a public resource of images for teaching and for the development and testing of automated diagnostic systems".

Performance evaluation on segmentation: normal and abnormal images using PH^2 database and ISIC database

Table 4 and Table 5 exhibit the segmentation performance of the proposed Improved K-means algorithm over the existing works in terms of both positive and negative measures using PH^2 database. Particularly, this evaluation resultants are acquired from both normal (Table 4) as well as abnormal (Table 5) dermoscopy images. In the case of the normal skin image in Table 4, the accuracy of the presented work is 0.86379 (higher), which is 47.83% and 0.245% better than the existing works like Conventional K-means (with no optimal centroid selection) and PA-MSA, respectively. This indicates that the proposed segmentation algorithm is capable of segmenting the regions more perfectly when compared to the traditional one. On the other hand, the negative measures depict the error performance, which is also a solution for the enhancement in the robustness of the presented work. The FNR of the presented work has the lowest value as 0.47513, which is 46.68 and 4.23% better than the existing works Conventional

Table 4: Segmentation performance of the presented work over the existing work for normal image using PH^2 database.

Measures	Conventional K-means (with no optimal centroid selection) [39]	PA-MSA [50]	Improved K-means with LANM based optimal centroid selection
Accuracy	0.45061	0.86167	0.86379
Sensitivity	0.10877	0.50388	0.52487
Specificity	0.54563	0.96113	0.95801
Precision	0.062392	0.78278	0.77651
FPR	0.45437	0.038868	0.041993
FNR	0.89123	0.49612	0.47513
NPV	0.54563	0.96113	0.95801
FDR	0.93761	0.21722	0.22349
F1_score	0.079298	0.6131	0.62636
MCC	−0.29386	0.55286	0.56254

Table 5: Segmentation performance of the presented work over the existing work for abnormal image using PH^2 database.

Measures	Conventional K-means (with no optimal centroid selection) [39]	PA-MSA [50]	Improved K-means with LANM based optimal centroid selection
Accuracy	0.385	0.75582	0.75921
Sensitivity	0.17308	0.4497	0.46542
Specificity	0.52195	0.95364	0.94906
Precision	0.1896	0.86241	0.85515
FPR	0.47805	0.046361	0.050943
FNR	0.82692	0.5503	0.53458
NPV	0.52195	0.95364	0.94906
FDR	0.8104	0.13759	0.14485
F1_score	0.18097	0.59114	0.60277
MCC	−0.31057	0.48815	0.49379

Table 6: Segmentation performance of the presented work over the existing work for normal image using ISIC database.

Measures	Conventional K-means (with no optimal centroid selection) [39]	PA-MSA [50]	Improved K-means with LANM based optimal centroid selection
Accuracy	0.347	0.8689	0.8964
Sensitivity	0.1654	0.5896	0.5987
Specificity	0.4695	0.9254	0.9685
Precision	0.07426	0.786	0.7985
FPR	0.5964	0.0345	0.02821
FNR	0.8694	0.4412	0.41457
NPV	0.6921	0.9493	0.95695
FDR	0.8963	0.25713	0.20242
F1_score	0.07694	0.62456	0.67245
MCC	−0.189	0.5111	0.5236

K-means (with no optimal centroid selection) and PA-MSA, respectively. On the other hand, the segmentation performance of the presented work over the existing work for the abnormal skin image is evaluated and the result is shown in Table 5. On observing the accuracy, the presented work has the highest accuracy as 0.75921, while the existing works are said to have the accuracy of Conventional K-means (with no optimal centroid selection)=0.385 and PA-MSA=0.75582. Thus, as a whole, the segmentation accuracy of the presented approach in case of segmentation is much better than the extant works. In certain cases, there might be a smaller deviation in the segmentation performance. But, as a whole, the disease detection accuracy of the presented approach from DCNN is still higher than the existing ones.

Table 6 and Table 7 show the segmentation performance of the proposed Improved K-means algorithm over the existing works in terms of both positive and negative measures using ISIC database. This evaluation resultants are acquired from both normal (Table 6) as well as abnormal (Table 7) skin images. Table 6 shows that for the normal skin image, the accuracy of the presented work is 0.8964 (higher), which is 61.289% and, 3.068% superior to the traditional methods like Conventional K-means (with no optimal centroid selection) and PA-MSA, correspondingly. Therefore, from the result, it is clear that the adopted segmentation algorithm is proficient of segmenting the regions more perfectly when compared to the traditional one. Moreover, the negative measures FPR of the proposed work has the lowest value as 0.02821, which is 95.270%, and 18.232% superior to the traditional methods Conventional K-means (with no optimal centroid selection) and PA-MSA, correspondingly. In addition, the segmentation performance of the Improved K-means algorithm over the existing work for the abnormal skin image is illustrated in Table 7. The accuracy, the proposed work has the highest accuracy as 0.75921, which is 51.55%, and 3.24% better than the existing works Conventional K-means (with no optimal centroid selection) and PA-MSA. In some cases, there might be a lesser variation in the segmentation performance, but the disease detection accuracy of the presented approach is much better than the existing works.

Table 7: Segmentation performance of the presented work over the existing work for abnormal image using ISIC database.

Measures	Conventional K-means (with no optimal centroid selection) [39]	PA-MSA [50]	Improved K-means with LANM based optimal centroid selection
Accuracy	0.3678	0.73455	0.75911
Sensitivity	0.1867	0.4464	0.4675
Specificity	0.5242	0.9513	0.9390
Precision	0.1422	0.86	0.85
FPR	0.47103	0.0411	0.03142
FNR	0.8256	0.55	0.5367
NPV	0.4642	0.9325	0.9589
FDR	0.8134	0.13	0.12346
F1_score	0.1856	0.5943	0.6120
MCC	−0.31	0.4814	0.48231

Overall performance: proposed vs. conventional models using PH^2 database and ISIC database

Table 8 exhibits the performance evaluation of the proposed melanoma detection framework (Improved K-mean

Table 8: Overall performance: proposed vs. conventional using PH^2 database.

	MI [1]		SVM [1]		PSO + NN [49]		CNN + SVM [51]		PS-MSA [50]		Proposed framework	
	Hold-out	Ten-fold	Hold-out	Ten-fold	Hold-out	Ten-fold	Hold-out	Ten-fold	Hold-out	Ten-fold	Hold-out	Ten-fold
Accuracy	0.71667	0.635	0.63333	0.635	0.525	0.63	0.71667	0.66	0.9	0.8875	0.93333	0.9375
Sensitivity	0.82857	0.80833	0.93333	0.80833	0.43137	0.74167	0.82759	0.75262	0.75	0.8875	0.83333	0.9875
Specificity	0.56	0.375	0.33333	0.375	0.68966	0.4625	0.6129	0.56734	1	0.8875	1	0.8875
Precision	0.725	0.65986	0.58333	0.65986	0.70968	0.67424	0.66667	0.66667	1	0.93889	1	0.93889
FPR	0.44	0.625	0.66667	0.625	0.31034	0.5375	0.3871	0.43266	0	0.1125	0	0.1125
FNR	0.17143	0.19167	0.066667	0.19167	0.56863	0.25833	0.17241	0.24738	0.25	0.1125	0.16667	0.0125
NPV	0.56	0.375	0.33333	0.375	0.68966	0.4625	0.6129	0.56734	1	0.8875	1	0.8875
FDR	0.275	0.34014	0.41667	0.34014	0.29032	0.32576	0.33333	0.33333	0	0.061111	0	0.061111
F1_Score	0.77333	0.72659	0.71795	0.72659	0.53659	0.70635	0.73846	0.69704	0.85714	0.89463	0.90909	0.95412
MCC	0.40638	0.20351	0.33333	0.20351	0.11942	0.21114	0.44932	0.31821	0.80178	0.87551	0.86603	0.92141

+ proposed LVP + DCNN) over the existing melanoma detection models like MI [1], SVM [1], PSO + MLP [49], PA-MSA [50] and CNN + NN [51] using PH^2 database. In the case of the holdout method, the datasets are fed randomly during both the testing and training, respectively. Further, in tenfold evaluation, the overall data set is split into 10 subsets, and they are trained and tested correspondingly. On observing the accuracy, the presented work has the highest accuracy in terms of both holdout and tenfold analysis. In the holdout method, the accuracy of the presented work is 0.93333 (highest), and it is 23.21, 32.14, 43.74, 23.21 and 3.57% better than the extant approaches like MI, SVM, PSO + NN, CNN + SVM and PS-MSA, respectively. Further, all the other positive measures like sensitivity, specificity and precision of the presented work are higher in the case of both holdout and tenfold analyses. The negative measures of the presented work are lower, while compared over the traditional works. In the case of FNR and FDR, the holdout performance of the presented work is the lowest value (0). Thus, from the overall evaluation, it is vivid that the presented work has the highest performance, and it is said to be more robust for melanoma prediction, while compared to the state-of-art techniques.

Table 9 shows the performance evaluation of the proposed melanoma detection framework over the existing melanoma detection models such as MI, SVM, PSO + MLP, PA-MSA and CNN + NN using ISIC database. On considering, the accuracy, the proposed work has the highest accuracy in terms of both holdout and tenfold analysis. The hold out the accuracy of the proposed work is 0.9095 (highest) and it is 16.86, 1.46, 16.86, 67.01 and 18.07% superior to than the existing models like MI, SVM, PSO + NN, CNN + SVM and PS-MSA, respectively. Hence, from the overall evaluation it is observed that the proposed model is said to be more robust for melanoma prediction, when compared to the state-of-art techniques.

Table 9: Overall performance: proposed vs. conventional models using ISIC database.

	MI [1]		SVM [1]		PSO + NN [49]		CNN + SVM [51]		PS-MSA [50]		Proposed framework	
	Hold-out	Ten-fold	Hold-out	Ten-fold	Hold-out	Ten-fold	Hold-out	Ten-fold	Hold-out	Ten-fold	Hold-out	Ten-fold
Accuracy	0.75619	0.5723	0.8962	0.6548	0.7562	0.8625	0.3	0.8654	0.74562	0.8658	0.9095	0.9256
Sensitivity	0.736914	0.74167	0.8692	0.7693	0.7987	0.94596	0.7856	0.8155	0.85697	0.7569	0.8796	0.97256
Specificity	0.671	0.81258	0.8756	0.6529	0.4796	1	0.32548	0	0.62135	1	0.3978	0.8965
Precision	0.692	0.5679	0.65	0.5462	0.8796	0.58963	0.65894	0.78134	0.9014	0.6344	0.5489	0.9456
FPR	0.4632	0.38164	0.42356	0.1	0.4569	0.34789	1	0.29856	0.3456	0.4579	0.1246	0.1546
FNR	0.06258	0.08689	0.08956	0.5035	0.3	0	0.01289	0.01356	0	0.0978	0	0.01524
NPV	0.692	0.3689	0.025	0.4689	0.2925	1	0.3478	0.4759	0.6892	0.8223	0.1563	0.86954
FDR	0.2359	0.2732	0.0236	0.54679	0.4567	0.8	0.02899	0.3549	0.0157	1	0.9862	0.05234
F1_Score	0.656456	0.2158	0.3249	0.8954	0.7214	0.5689	0.7	0.6987	0.8956	0.2314	1	0.93648
MCC	0.56921	0.22361	0.44762	0.13548	0	0.4568	0.54760	0.1	0.8796	0.1715	0.86695	0.95343

Conclusion

A novel melanoma detection framework was developed in the current research work by following the three major phase's viz. segmentation, feature extraction and detection. In the segmentation phase (initial phase), the initial centroids were selected optimally by a new Improved K-means clustering. As a novelty, here the centroids are optimally tuned by a new algorithm termed LANM, which was based on the consideration of multi-objective including intensity diverse centroid, spatial map and frequency of occurrence, respectively. In the feature extraction phase, the proposed NVLVP features as well as GLCM were extracted from the segmented image. Further, these extracted features were fed as input to DCNN for melanoma detection. Finally, the performance of the proposed model is evaluated over other conventional models by determining both the positive as well as negative measures. In the case of the normal skin image, the accuracy of the presented work is 0.86379 (higher), which is 47.83 and 0.245% better than the existing works like Conventional K-means (with no optimal centroid selection) and PA-MSA, respectively. On observing the accuracy of abnormal skin image, the presented work has the highest accuracy as 0.75921, while the existing works are said to have the accuracy of Conventional K-means (with no optimal centroid selection)=0.385 and PA-MSA=0.75582. In the future, the number of melanocytic lesion types can be extended for an improved evaluation of melanocytic lesion to reduce the amount of dermoscopic pitfalls.

Research funding: None declared.
Author contributions: All the authors have accepted responsibility for the entire content of this submitted manuscript and approved submission.
Competing interests: The authors declare that they have no conflict of interest.
Employment or leadership: None declared.
Ethical Approval: The conducted research is not related to either human or animal use.

References

1. Do T, Hoang T, Pomponiu V, Zhou Y, Chen Z, Cheung NM, et al. Accessible melanoma detection using smartphones and mobile image analysis. IEEE Trans Multimed 2018;20: 2849–64.
2. Hekler A, Utikal JS, Enk AH, Hauschild A, Collaborators. Superior skin cancer classification by the combination of human and artificial intelligence. Eur J Cancer 2019;120:114–21.
3. Risica PM, Matthews NH, Dionne L, Mello J, Weinstock MA. Psychosocial consequences of skin cancer screening. Prev Med Rep 2018;10:310–6.
4. Bhattacharjee P, Das A, Ashok K, Pritha Bhattacharjee G. Epigenetic regulations in alternative telomere lengthening: understanding the mechanistic insight in arsenic-induced skin cancer patients. Sci Total Environ 2020;704:135388.
5. Warsi F, Khanam R, Kamya S, Paz Suárez-Araujo C. An efficient 3D color-texture feature and neural network technique for melanoma detection. Inf Med Unlocked 2019;17:100176.
6. Mirbeik-Sabzevari A, Tavassolian N. Ultrawideband, stable normal and cancer skin tissue phantoms for millimeter-wave skin cancer imaging. IEEE (Inst Electr Electron Eng) Trans Biomed Eng 2019;66:176–86.
7. Keshavarz A, Vafapour Z. Water-based terahertz metamaterial for skin cancer detection application. IEEE Sensor J 2019;19: 1519–24. Feb 15, 2019.
8. Zhou Y, Herman C. Optimization of skin cooling by computational modeling for early thermographic detection of breast cancer. Int J Heat Mass Tran 2018;126:864–76.
9. Yang Y, Wu R, Sargsyan D, Yin R, Kong A-N. UVB drives different stages of epigenome alterations during progression of skin cancer. Canc Lett 2019;449:20–30.
10. Zhang F, Jin T, Hu Q, He P. Distinguishing skin cancer cells and normal cells using electrical impedance spectroscopy. J Electro Anal Chem 2018;823:531–6.
11. Geetharamani G, Aathmanesan T. Split ring resonator inspired THz antenna for breast cancer detection. Optic Laser Technol 2020;126:106111.
12. Dascalu A, David EO. Skin cancer detection by deep learning and sound analysis algorithms: a prospective clinical study of an elementary dermoscope. EBio Med 2019;43:107–13.
13. Gordon LG, Brynes J, Baade PD, Neale RE, Janda M. Cost-effectiveness analysis of a skin awareness intervention for early detection of skin cancer targeting men older than 50 years. Value Health 2017;20:593–601.
14. Rahman A, Rahman AK, Rao B. Early detection of skin cancer via terahertz spectral profiling and 3D imaging. Biosens Bioelectron 2016;82:64–70.
15. Maron RC, Weichenthal M, Utikal JS, Hekler A, Collabrators. Systematic outperformance of 112 dermatologists in multiclass skin cancer image classification by convolutional neural networks. Eur J Cancer 2019;119:57–65.
16. Fusco P, Cofini V, Petrucci E, Scimia P, Paladini G, Behr AU, et al. Unilateral paravertebral block compared with subarachnoid anesthesia for the management of postoperative pain syndrome after inguinal herniorrhaphy: a randomized controlled clinical trial. Pain 2016;157:1105–13.
17. Bonacaro A, Rubbi I, Sookhoo D. The use of wearable devices in preventing hospital readmission and in improving the quality of life of chronic patients in the homecare setting: a narrative literature review. Prof Inferm 2019;72:31550431.
18. Massoudi AH, Jameel AS, Ahmad AR. Stimulating organizational citizenship behavior by applying organizational commitment and satisfaction. Int J Soc Sci Econ Rev 2020;2:20–7.
19. Zhou Y, Herman C. Optimization of skin cooling by computational modeling for early thermographic detection of breast cancer. Int J Heat Mass Tran 2018;126:864–76.

20. Zhang L, Ji Z, Zhang J, Yang S. Photodynamic therapy enhances skin cancer chemotherapy effects through autophagy regulation. Photodiagnosis Photodyn Ther 2019;28:159–65.
21. Garcia MR, Requena MB, Pratavieira S, Tan Moriyama L, Magalhães DV. Development of a system to treat and online monitor photodynamic therapy of skin cancer using PpIX near-infrared fluorescence. Photodiagnosis Photodyn Ther 2020; 30:101680.
22. Vilanova Garcia D, da Silva Filho JI, Silveira L, Tavares Pacheco MT, Mario MC. Analysis of Raman spectroscopy data with algorithms based on paraconsistent logic for characterization of skin cancer lesions. Vib Spectrosc 2019;103:102929.
23. Ravi RV, Subramaniam K. Image compression and encryption using optimized wavelet filter bank and chaotic algorithm. Int J Appl Eng Res 2017;12:10595–610.
24. Thangam T, Kazem HA, Muthuvel K. SFOA: sun flower optimization algorithm to solve optimal power flow. Resbee Publishers.
25. Rajakumar BR. Static and adaptive mutation techniques for genetic algorithm: a systematic comparative analysis. Int J Comput Sci Eng 2013;8:180–93.
26. Thomas R, Rangachar MJS. Hybrid optimization based DBN for face recognition using low-resolution images. Multimed Res 2018;1:33–43.
27. Bossolasco M, Maria Fenoglio L. Yet another PECS usage: a continuous PECS block for anterior shoulder surgery. J Anaesthesiol Clin Pharmacol 2018;34:569.
28. Manassero A, Bossolasco M, Ugues S, Bailo C. An atypical case of two instances of mepivacaine toxicity. J Anaesthesiol Clin Pharmacol 2014;30:582.
29. Nipanikar SI, Hima Deepthi V. Enhanced whale optimization algorithm and wavelet transform for image stenography. Multimed Res 2019;2:23–32.
30. Vinolin V. Breast cancer detection by optimal classification using GWO algorithm. Multimed Res 2019;2:10–8.
31. Nida N, Irtaza A, Ali J, Yousaf MH, Mahmood MT. Melanoma lesion detection and segmentation using deep region based convolutional neural network and fuzzy C-means clustering. Int J Med Inf 2019;124:37–48.
32. Thanh DNH, Surya Prasath VB, Hieu NN. Melanoma skin cancer detection method based on adaptive principal curvature, colour normalisation and feature extraction with the ABCD rule. J Digit Imag 2020;33:574–85.
33. Tan TY, Zhang L, Lim CP. Intelligent skin cancer diagnosis using improved particle swarm optimization and deep learning models. Appl Soft Comput 2019;84:105725.
34. Mirbeik-Sabzevari A, Li S, Garay E, Nguyen H, Wang H, Tavassolian N. Synthetic ultra-high-resolution millimeter-wave imaging for skin cancer detection. IEEE (Inst Electr Electron Eng) Trans Biomed Eng 2019;66:61–71.
35. Tan TY, Zhang L, Chin Neoh S, Lim CP. Intelligent skin cancer detection using enhanced particle swarm optimization. Knowl Base Syst 2018;158:118–35.
36. Zhang N, Cai Y-X, Wang Y-Y, Tian Y-T, Badami B. Skin cancer diagnosis based on optimized convolutional neural network. Artif Intell Med 2020;102:101756.
37. Jaworek-Korjakowska J, Kłeczek P. Automatic classification of specific melanocytic lesions using artificial intelligence. BioMed Res Int 2016. https://doi.org/10.1155/2016/8934242.
38. Goyal M, Oakley A, Bansal P, Dancey D, Yap MH. Skin lesion segmentation in dermoscopic images with ensemble deep learning methods. IEEE Access 2019;8:4171–81.
39. Anton N, Arponen O, Aki N, Masarwah A, Anna S, Liimatainen T, et al. Quantitative volumetric K-means cluster segmentation of fibroglandular tissue and skin in breast MRI. J Digit Imag 2018;31: 425–34.
40. Boothalingam R. Optimization using lion algorithm: a biological inspiration from lion's social behavior. Evol Intell 2018;11:31–52.
41. Rajakumar BR. Optimization using lion algorithm: a biological inspiration from lion's social behavior. Evol Intell, Special Issue on Nature inspired algorithms for high performance computing in computer vision 2018;11:31–52.
42. Rajakumar BR. Lion algorithm for standard and large scale bilinear system identification: a global optimization based on Lion's social behavior. Beijing, China: IEEE Congress on Evolutionary Computation; 2014:2116–23 pp.
43. Rajakumar BR. The Lion's algorithm: a new nature inspired search algorithm. In Procedia Technology-2nd International Conference on Communication, Computing & Security, vol 6; 2012:126–35 pp. (Elsevier).
44. Rajakumar BR. Lion algorithm and its applications. In: Khosravy M, Gupta N, Patel N, Senju T, editors. Frontier applications of nature inspired computation in Springer tracts in nature-inspired computing (STNIC). Springer; 2020.
45. Fan K-C, Hung T-Y. A novel local pattern descriptor—local vector pattern in high-order derivative space for face recognition. IEEE Trans Image Proc 2014;23:2877–91.
46. Properties of variance. Available from: https://en.wikipedia.org/wiki/Qualitative_variation [Accessed 13 05 2020].
47. Arabi PM, Joshi G, Deepa NV. Performance evaluation of GLCM and pixel intensity matrix for skin texture analysis. Perspect Sci 2016;8:203–6.
48. Gu J, Wang Z, Kuen J, Ma L, Shahroudy A, Shuai B, et al. Recent advances in convolutional neural networks. Pattern Recogn 2018; 77:354–77.
49. Mukherjee S, Adhikari A, Roy M. Malignant melanoma detection using multilayer perceptron with optimized network parameter selection by PSO. In Contemporary advances in innovative and applicable information technology; 2018;812:101–9.
50. Sukanya. Deep learning based melanoma detection with optimized features via hybrid algorithm. In Communication; 2019.
51. Jadhav AR, Ghontale AG, Shrivastava VK. Segmentation and border detection of melanoma lesions using convolutional neural network and SVM. In Computational Intelligence: Theories, Applications and Future Directions; 2018, vol 1:97–108 pp.